Electronic structure and thermal decomposition of 5-aminotetrazole studied by UV photoelectron spectroscopy and theoretical calculations

ARTICLE *in* CHEMICAL PHYSICS · MARCH 2011

Impact Factor: 1.65 · DOI: 10.1016/j.chemphys.2011.01.008

3 AUTHORS:

Rui M. Pinto
INESC Microsistemas e Nanotecnologias
19 PUBLICATIONS **66** CITATIONS
SEE PROFILE

A.A. Dias
New University of Lisbon
27 PUBLICATIONS **227** CITATIONS
SEE PROFILE

Maria Lourdes Costa
New University of Lisbon
48 PUBLICATIONS **435** CITATIONS
SEE PROFILE

Electronic structure and thermal decomposition of 5-aminotetrazole studied by UV photoelectron spectroscopy and theoretical calculations

Rui M. Pinto[a,*], António A. Dias[a], Maria L. Costa[a]

[a] *CFA, Centro de Física Atómica, Departamento de Física, Faculdade de Ciências e Tecnologia, FCT, Universidade Nova de Lisboa, 2829-516 Caparica, Portugal*

Abstract

The electronic properties and thermal decomposition of 5-aminotetrazole (5ATZ) are investigated using UV photoelectron spectroscopy (UVPES) and theoretical calculations. Simulated spectra of both 1H- and 2H-5ATZ, based on electron propagator methods, are produced in order to study the relative gas-phase tautomer population. The thermal decomposition results are rationalized in terms of intrinsic reaction coordinate (IRC) calculations. 5ATZ yields a HOMO ionization energy of 9.44±0.04 eV and the gas-phase 5ATZ assumes mainly the 2H-form. The thermal decomposition of 5ATZ leads to the formation of N_2, HN_3 and NH_2CN as the primary products, and HCN from the decomposition of a intermediate CH_3N_3 compound. The reaction barriers for the formation of HN_3 and N_2 from 2H-5ATZ are predicted to be ≈228 and ≈150 kJ/mol, at the G2(MP2) level, respectively. The formation of HCN and HNNH from the thermal decomposition of a CH_3N_3 carbene intermediate is also investigated.

Keywords: 5-aminotetrazole, Photoelectron spectroscopy, Thermal decomposition, IRC calculations

1. Introduction

Tetrazoles [1] (CN_4H_2) are exceedingly important compounds due to their practical role in different industrial and medical applications.

In industry, tetrazole derivatives are of common use and newly synthesized compounds [2] offspring from research at a frequent pace. They present appealing tribological functionalities if coupled to some active elements, functioning as an additive to liquid paraffin, in applications where anti-wear and friction reduction oils are needed [3]. In addition, its use as a corrosion inhibitor in copper polishing has also been reported [4]. Also, its thermal stability in conjunction with the high nitrogen content, lead to its use in safer and environment-friendly explosives and pyrotechnics [5–7].

In medicine, the tetrazole ring is present in a wide range of drugs [8, 9], acting as a powerful isosteric substituent of the carboxylic group, -CO_2H, with the advantage of being metabolically more stable than the latter [10, 11].

From a fundamental point-of-view, some tetrazoles are best known for exhibiting annular tautomerism, a characteristic which has been studied both through a myriad of theoretical methods[12–14] and several experiments based on NMR [15, 16], IR [17–19] and UV photoelectron [20] spectroscopies and mass spectrometry [21, 22]. These studies suggest that both 1H- and 2H-forms can coexist in the gas-phase, the 2H-tautomer being predominant over the 1H-tautomer, in the vast majority of simple tetrazole based molecules; it is also a matter of overall agreement that the nature of the 5-substituent affects the tautomeric equilibrium of the tetrazole ring.

5-aminotetrazole (5ATZ, NH_2CN_4H, Fig. 1) is a perfect example of a tetrazole derivative. It is widely used as an intermediate in the synthesis of tetrazole compounds because of its assorted reactions and ease of preparation. Its nitrogen content is rated above 82.3 wt % and it is considered a high-energetic material [5–7].

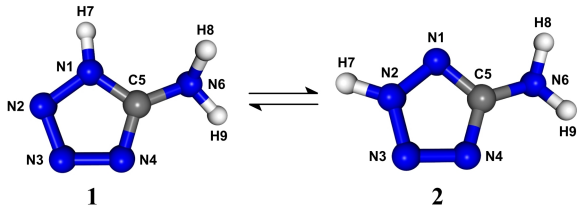

Figure 1: 1H-form and 2H-form of 5ATZ (**1** and **2**, respectively).

Fundamental experimental research on 5ATZ is mainly based on thermal decomposition analysis with subsequent tautomeric equilibrium evaluation, through the assessment of the intermediates associated with the different decomposition pathways [23–26]. To our knowledge, the only experimental study trying to characterize the outer-valence electronic structure of 5ATZ is the work by Sun et al. [27], using ultraviolet photoelectron spectroscopy (UVPES). However, there is no mention to the preferable tautomeric form adopted by this molecule, and an incomplete assignment is done based on calculations on the 1H-tautomer only.

Levchik et al. [23], using different spectroscopic methods, analyzed the thermal degradation of 5ATZ between 25 and 700 °C. They argued that heating the intact solid sample to a temperature near its melting point (≈201°C) and quenching it to room

*Corresponding author.
Email address: ruipinto@fct.unl.pt (Rui M. Pinto)

temperature, or evaporating it under vacuum lead to an increase of the amino form. Interdependent parallel routes for the thermal decomposition of 5ATZ were proposed, which accounted for the formation of hydrogen azide (HN_3) plus cyanamide (NH_2CN), and for the formation of N_2 plus a metastable CH_3N_3 product. Brill and Ramanathan [24] studied the chemical pathways behind 5ATZ thermal decomposition, by using temperature jump/Fourier transform IR (T-Jump/FTIR) spectroscopy and analyzing the gaseous final products of the flash pyrolysis of 5ATZ, at 350 °C, 400 °C and 450 °C. The authors have shown that the evaporation of intact 5ATZ resulted in HN_3 and NH_2CN.

Lesnikovich et al. [25] used several thermal analysis methods, associated with gas-cromatography mass-spectrometry (GC/MS) and FTIR spectroscopy, to shed light on the kinetics and thermal decomposition mechanisms of aminotetrazoles, including 5ATZ. Originating from the thermal decomposition of 5ATZ, the compounds N_2, HN_3 and NH_3 were identified among the gaseous products, and ammonium azide (NH_4N_3) and melamine were found among the volatile condensed products. Lesnikovich et al. [25] also pointed out that the heating or evaporation of 5ATZ resulted in a population increase of the amino form.

Finally, the recent work of Paletsky et al. [26] presents results for the kinetics of 5ATZ thermal decomposition, at high heating rates (50 – 275 °C/s). In agreement with the results from the above mentioned references, Paletsky et al. [26] also identify HN_3, N_2, NH_2CN, HCN, NH_3 and 5ATZ vapor as the products formed upon thermal decomposition of 5ATZ.

The theoretical studies [28–30] on the thermal decomposition of 5-ATZ (and its imino form, 5ITZ) by Zhang et al. [28], Kiselev and Gritsan [29] and Paul et al. [30], give a crucial insight on the interpretation of the data arising from thermal decomposition experiments. Zhang et al. [28] have studied the kinetics of decomposition of 1H-5ATZ to HN_3 and NH_2CN, presenting intrinsic reaction coordinate (IRC) curves connecting the reactants, the transition structures (TS) and the products.

The work by Kiselev and Gritsan [29] covered the thermal decomposition and isomeric interconversion of 1H-, 2H-5ATZ and 5ITZ, by analyzing most of the decomposition pathways for the three isomers. Conclusions show that the imino form is prone to the fast bimolecular conversion to the more thermodynamically preferable 1H-5ATZ tautomer. HN_3, N_2, NH_2CN, carbodiimide, 3-imino-diaziridin, an azide intermediate (NH_2NHCN_3) leading also to a metastable CH_3N_3 compound, and a carbene are pointed out as possible decomposition products from unimolecular reactions.

Paul et al. [30] also studied the unimolecular thermal decomposition reactions of 1H-, 2H-5ATZ and 5ITZ by isopotential searching. According to the authors, 5ITZ can decompose through two different routes: formation of HN_3 plus NH_2CN, and formation of N_2 plus 3-imino-diazirin. This study suggested that 3-imino-diazirin readily decomposes into hydrogen isocyanide (HNC) and *trans*-diazene (HNNH). Furthermore, Paul et al. [30] also show that the decomposition of 1H-5ATZ and 2H-5ATZ leads to the formation of HN_3, N_2, NH_2CN, HN=C=NH and a metastable CH_3N_3 product, in agreement with Kiselev and Gritsan [29].

In order to study the electronic structure of 5ATZ, we elect the UVPES technique as the primary method of accessing the ionization energy values and band profiles, paying special attention to the tautomerism issue, a matter which can also be evaluated through UVPES [20, 31, 32]. Contrary to Sun et al. [27], both 5ATZ tautomers are studied by theoretical calculations, in order to correctly assign the gas-phase photoelectron spectrum of 5ATZ.

UVPES is also used for studying the thermal decomposition of 5ATZ, by means of a molecular oven, specifically built for this task. The decomposition routes are thoroughly followed by IRC calculations, which further rationalize and clarify the experimental results, definitively unveiling the intricate mechanisms behind the thermal decomposition of this tetrazole based compound.

2. Experimental method

The UV photoelectron spectrometer used to record the spectra is very similar to the one described elsewhere [33]. An illustrated view of the apparatus is given in Fig. 2. It operates under high vacuum conditions and it consists of a large 150° spherical sector electrostatic analyzer (mean radius = 200 mm) and a DC discharge lamp, capable of producing He(I) (21.22 eV) radiation. Typical working resolution is 30 meV full width at half maximum (FWHM) as measured at the $Ar^+ \, ^2P_{3/2} \leftarrow Ar \, (^1S_0) \, (3p)^{-1}$ band.

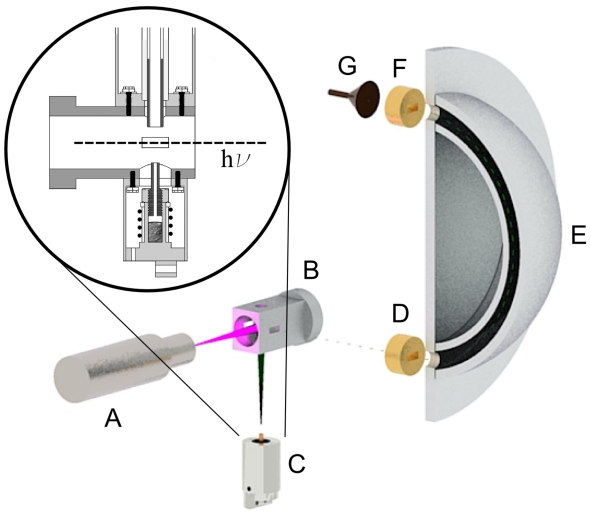

Figure 2: Schematics of the experimental setup, with an expanded view of the resistively heated oven: A - UV source, B - reaction cell, C - oven, D - entrance slits, E - energy analyzer, F - exit slits and G - electron detector.

As 5ATZ is a crystalline solid at room temperature, we designed and used a resistively heated oven to evaporate the sample (Fig. 2, C). The heating resistance is powered by a DC power supply which is coupled to a solid state relay (SSR) and a PID controller. The feedback signal is the temperature read at the nozzle of the oven, with a type J (Fe/Cu-Ni) thermocouple.

A LabView program drives the PID and sets the oven temperature, which remains stable to within 0.2 °C around the desired value. The internal space available for the evaporating charge is 0.35 cm^3 and the oven tip is made of stainless steel, with an internal diameter of 1.0 mm and a length of 20.0 mm.

In order to obtain photoelectron (PE) spectra of 5ATZ (*Aldrich*, 97%, mp = 201°C), with no traces of the thermal decomposition products, the tip with the largest ID was used (3.0 mm), and the heating process was conducted at low heating rates (< 60 °C/min), in 10 °C steps, until a temperature close to the melting temperature was reached. The temperature was then increased in 2 °C steps until a sufficient signal was obtained. Experimental vertical ionization energies (VIEs) were calibrated by addition of a small amount of argon and by traces of water present in the sample [34].

For the thermal decomposition studies, tips with different IDs were experimented in order to maintain the pressure below maxima workable values ($\approx 2 \times 10^{-4}$ mbar), inside the reaction chamber. The heating process was also conducted with caution, by slowly increasing the temperature, in 10 or 5 °C steps, at low heating rates. The thermal decomposition spectra were calibrated using the ionization lines associated with the final decomposition products (N_2, HCN and HN_3).

3. Computational details

The framework for our theoretical studies on 5ATZ is based on the one-electron propagator description [35] of the molecular system, implemented at the level of outer-valence Green's function (OVGF) and partial third-order (P3) schemes [36, 37]. These methods have already proven to be an invaluable tool in the study of PE spectra of several molecules [32, 38, 39], up to the one-electron picture breakdown.

The structures and total energies presented in this work were obtained with the Hartree-Fock (HF) method [40], second-order Møller-Plesset (MP2) perturbation theory [41] and density-functional theory (DFT) [42], together with the split-valence double- and triple-ζ basis sets [43], 6-31+G(d) and 6-311++G(d,p), with added diffuse and polarized functions. DTF results were obtained with Becke's hybrid three parameter exchange functional [44] along with the Lee, Yang and Parr correlation functional [45].

Initial geometry optimization of the isomeric forms of 5ATZ was computed with the modest HF/6-31+G(d) procedure, followed by a more refined optimization at MP2/6-311++G(d,p) and DFT B3LYP/6-311++G(d,p) levels of theory. No symmetry restrictions were imposed in these optimizations. The OVGF/6-311++G(d,p) and P3/6-311++G(d,p) calculations were performed on the fully optimized geometries obtained with MP2/6-311++G(d,p), within the frozen-core approximation.

The optimized geometries of the cations of 1H- and 2H-5ATZ were calculated with the unrestricted B3LYP method (UB3LYP), maintaining the same basis set used in the computations for the neutral species (6-311++G(d,p)).

The thermochemical data regarding 1H-, 2H-5ATZ and 5ITZ were calculated with the hybrid G2(MP2) method [46]. Estimates of relative populations of tautomers at the evaporation temperature of 1H- and 2H-5ATZ, were based on the Boltzmann distribution formula:

$$n_i = \frac{e^{-(G_i - G_0)/kT}}{\sum_n e^{-(G_n - G_0)/kT}} \quad (1)$$

where n_i is the population ($\in [0, 1]$) of the ith tautomer, G_i is the Gibbs energy of the ith tautomer, G_0 the Gibbs energy of the most stable tautomer and T the desired temperature. The resulting populations are designated by Boltzmann population ratios (BPR).

Regarding the thermal decomposition pathways, we have carried out several calculations, based on a simple 4-step procedure: **(i)** a relaxed potential energy surface (PES) scan along the bond of interest, in order to detect a possible TS; **(ii)** the full optimization and validation of the candidate TS; **(iii)** a IRC calculation starting from this TS, connecting reactant, TS and products; and finally, **(iv)** the full optimization of the final products. Steps **i** and **iii** were calculated with MP2(Full)/6-31G(d), and steps **ii** and **iv** with the G2(MP2) method.

It should be pointed out that, although the G2(MP2) results presented in this work include zero-point energy (ZPE) and thermal enthalpy corrections, the important and emergent question of basis set superposition error (BSSE) [47–49] is not addressed. Standard Counterpoise (CP) corrections or the use of a local MP2 method could help estimate/minimize the BSSE value. Eventually, for maximum accuracy in relative energy differences, the focal-point analysis (FPA) is the solution of choice [14].

All calculations were carried out using the Gaussian 09 suite of programs [50]. For each tautomer, the computed VIEs obtained at OVGF/6-311++G(d,p)//MP2/6-311++G(d,p) and P3/6-311++G(d,p)//MP2/6-311++G(d,p) levels were convoluted with Lorentzian functions of 0.4 eV FWHM [51] and summed over to generate the corresponding simulated spectrum.

4. Results and discussion

4.1. Structures and molecular orbitals of 5ATZ

The full optimized structures of the two 5-aminotetrazole tautomers, 1H- and 2H-5ATZ, in the neutral ground state, obtained at the MP2/6-311++G(d,p) and B3LYP/6-311++G(d,p) levels of theory, are shown in Table 1.

Both MP2 and B3LYP methods present similar structural parameters, with differences no greater than 0.05 Å for bond lengths and 1.5° for angle values. With the exception of the hydrogen (H8) that is positioned on the same side of the 1-substituent (H7), all the atoms forming 1H-5ATZ neutral reside in same plane. In terms of symmetry, 1H-5ATZ belongs to the trivial C_1 group.

The re-positioning of the hydrogen substituent on the tetrazole ring slightly affects the opening of the cyclic structure. Changing the hydrogen position from 1 to 2, increases the N1-N2-N3 and the N4-C5-N1 angles in 10° and 5°, respectively.

Table 1: Calculated geometric parameters (Å, deg) for the 1H- and 2H-tautomer of 5ATZ, with two different methods and the 6-311++G(d,p) basis.

	1H-5ATZ		2H-5ATZ	
Parameter	MP2	B3LYP	MP2	B3LYP
r_{N1N2}	1.350	1.368	1.325	1.338
r_{N2N3}	1.313	1.280	1.334	1.317
r_{N3N4}	1.360	1.362	1.329	1.308
r_{N4C5}	1.324	1.319	1.353	1.362
r_{C5N1}	1.352	1.350	1.348	1.330
r_{NH}	1.011	1.010	1.012	1.010
r_{CNH_2}	1.385	1.372	1.381	1.371
α_{N1N2N3}	105.6	105.8	115.8	114.8
α_{N2N3N4}	111.1	111.9	104.8	106.0
α_{N3N4C5}	106.1	105.9	106.3	106.3
α_{N4C5N1}	108.0	108.2	113.0	112.6
α_{N1C5N6}	124.5	125.5	123.4	124.5

In addition, as H7 is placed farther away in the ring, the interaction between it and the amino group's hydrogen (H8) diminishes, placing the latter closer to the tetrazole containing plane. As with the 1H-tautomer, 2H-5ATZ also belongs to the C_1 symmetry group.

The optimized structures of the 1H- and 2H-5ATZ cations were obtained with the unrestricted B3LYP/6-311++G(d,p) method/basis. The major differences between the cationic and neutral geometric parameters of both tautomers of 5ATZ are displayed in Table 2. Based on these results, elongations of bonds N2-N3 and N4-C5 and shortening of the substituent bond (C5-R) should accompany the ionization process. Also, the loss of an electron raises the symmetry of both tautomers to C_s.

Table 2: Differences between selected geometric parameters (Å) of the tautomers of 5ATZ in cationic and neutral ground states, obtained with B3LYP/6-311++G(d,p). R = NH_2.

Difference	1H-5ATZ$^+$	2H-5ATZ$^+$
Δr_{N1N2}	-0.045	-0.052
Δr_{N2N3}	0.085	0.080
Δr_{N3N4}	-0.076	-0.043
Δr_{N4C5}	0.061	0.028
Δr_{C5-R}	-0.062	-0.055

Fig. 3 depicts the contours of selected MOs (isovalue=0.07) of 1H- and 2H-5ATZ, based on MP2/6-311++G(d,p) results. The highest occupied molecular orbitals (HOMOs) of 1H- and 2H-5ATZ are both very similar π orbitals originating from the atoms that constitute the tetrazole ring (π_{N4-C5} and π_{N2-N3}). MO 21a of the 1H-tautomer is formed by a π lone pair (LP) originated at N1 (π_{LPN1}) and by the two π contributions from the two opposite nitrogens (π_{N3-N4}). In the 2H-tautomer, this π_{LPN1} coalesces with the adjacent π_{N2} orbital, forming a π_{N1-N2} MO. The next orbital in both tautomers, MO 20a, is largely formed from two lone pair orbitals, σ_{LPN3} and σ_{LPN4}, even tough the

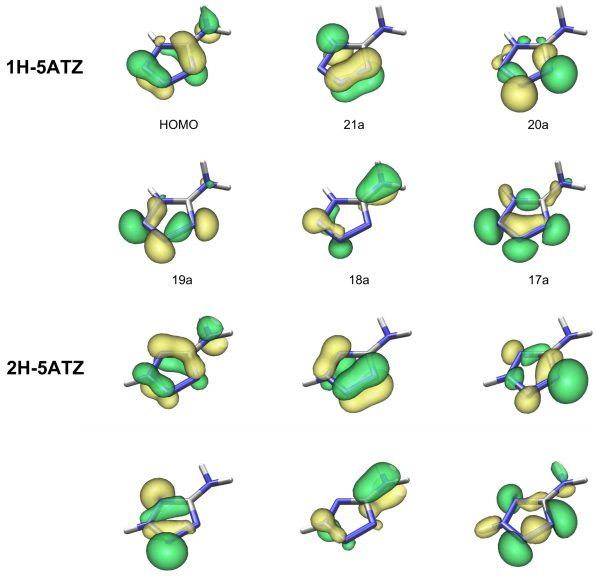

Figure 3: Molecular orbitals contours (isovalue = 0.07) of 1H- and 2H-5ATZ, from MP2/6-311++G(d,p) results.

contribution from the σ_{LPN3} in 2H-5ATZ appears to a lesser extent than in 1H-5ATZ. Orbital 19a of 1H-5ATZ consists of three LPs, coming from three consecutive atoms in the tetrazole ring (N2, N3 and N4), mixed with σ bondings between N1-N2 and N3-N4. A more symmetric distribution takes place in the 19a MO of the 2H-tautomer, where two opposite LPs (σ_{LPN1}, σ_{LPN3}) compose the MO. In both tautomers, 18a is a π orbital bonding the carbon and the nitrogen from the amino group (π_{C5-N6}). Finally, orbital 17a in both tautomers comes from different patterns of three σ LPs of the tetrazole nitrogens, with small amounts of σ contributions from the remaining atoms.

4.2. Total energies and thermochemistry

The total and relative electronic energies of 1H-5ATZ and 2H-5ATZ obtained with different methods and basis are displayed in Table 3. In addition to our results, other references are given, for the sake of comparison [25, 30, 52, 53].

As expected, 2H-5ATZ lies lower in energy than the 1H-tautomer, within all theory levels. B3LYP/6-311++G(d,p) places the latter tautomer 15.1 kJ/mol above the 2H form, whereas MP2/6-311++G(d,p) raises this difference to 22.3 kJ/mol. The more accurate G2(MP2) method settles this value to 12.1 kJ/mol, approximately. Comparison of the G2(MP2) energy with the single point energy obtained from the high-end coupled cluster method (CCSD(T)) [30], upon a fully optimized B3LYP/6-311++G(d,p) structure, shows that G2(MP2) is a very accurate method, with the advantage of being computationally less demanding.

In order to obtain the relative abundance of the 1H- and 2H-tautomers of 5ATZ, at room temperature (T≈298 K) and at the compound approximate melting temperature (T≈460 K), the G2(MP2) Gibbs free energies were used in conjunction with Eq. 1. The results are shown in Table 4.

Table 3: Total (hartree) and relative (kJ/mol) electronic energies of 1H- and 2H-5ATZ, calculated at different levels of theory.

	Total Energy		ΔE_{1H-2H}
Method/basis	1H-5ATZ	2H-5ATZ	kJ/mol
MP2/6-31G(d,p)[a]	-312.759013	-312.766312	19.16
MP2/6-311++G(d,p)	-312.888254	-312.896752	22.31
B3LYP/6-31G(d)[b]	-313.608830	-313.613980	13.52
B3LYP/6-31++G(d,p)[c]	-313.635719	-313.641361	14.81
B3LYP/6-311++G(d,p)	-313.705810	-313.711580	15.15
CCSD(T)/aug-cc-pVTZ			
//B3LYP/6-311++G(3df,3pd)[d]	-313.156788	-313.161212	11.61
G2(MP2)	-313.142366	-313.146959	12.06

[a]Ref. [25], [b]Ref. [52], [c]Ref. [53] and [d]Ref. [30]

Table 4: Gibbs free energies ($G_{G2(MP2)}$, a.u.), relative energies (ΔG, kJ/mol) and Boltzmann population ratios (BPR, %) of 1H- and 2H-5ATZ.

	T=298 K			T=460 K		
Tautomer	$G_{G2(MP2)}$	ΔG	BPR	$G_{G2(MP2)}$	ΔG	BPR
2H-5ATZ	-313.179643	0.0	99.0	-313.199190	0.0	94.7
1H-5ATZ	-313.175281	11.5	1.0	-313.194972	11.1	5.3
5ITZ	-313.157839	57.2	-	-313.177829	56.1	-

The optimized structure and energy of the imino tautomer (5-iminotetrazole, 5ITZ) was also obtained at the G2(MP2) level, to check whether it could really be excluded from comparison with the other two tautomers, in terms of energy and stability. The results place the imino form 56.1 kJ/mol above the lowest energy tautomer (2H-5ATZ), which corresponds to a very low BPR, relatively to the more stable 1H- and 2H-forms. At 460 K, the 2H-tautomer is predominant over the 1H-form, with 94.7% of the 5ATZ population assuming this configuration.

4.3. Photoelectron spectrum of 5ATZ

Assignment of the experimental PE spectra of 5ATZ is supported by calculations performed at the OVGF/6-311++G(d,p) and at the P3/6-311++G(d,p) levels over the fully optimized MP2/6-311++G(d,p) 1H- and 2H-tautomer structures. These results are shown in Table 5 and Table 6, together with the main character of the first six HOMOs and the MP2 energies obtained with the same basis set. The pole strengths associated with all VIEs from P3 and OVGF B calculations fall between 0.85 and 0.91.

The PE spectrum of 5ATZ, taken at 190 °C, is presented in Fig. 4, section (a), where the bands are labeled A-E and the asterisk marks the N_2 trace from a controlled leak. Our spectrum follows the same pattern as the only spectrum reported previously in the literature [27], with a broad first peak (A) centered at 9.44 eV, some vibrational structure on top of it and a pronounced shoulder on the right side. This peak corresponds to the ionization of the HOMO, a $\pi_{N4-C5,N2-N3}$ plus the amino π lone pair from N6. P3 results for this first ionization energy (IE) give 9.51 eV, taken from calculations upon the 2H-tautomer,

Table 5: Calculated vertical ionization energies (VIE, in eV) of 1H-5ATZ

		1H-5ATZ		
		MP2	OVGF[a]	P3[a]
MO	Character	VIE	VIE	VIE
22a	$\pi_{N4-C5,N2-N3}$	10.29	9.75	10.09
21a	$\pi_{N3-N4,LPN1}$	12.41	10.79	11.04
20a	$\sigma_{LPN3,LPN4}$	12.68	11.11	11.36
19a	$\sigma_{LPN2,LPN3,LPN4}$	12.93	11.48	11.73
18a	π_{C5-N6}	14.37	12.91	12.97
17a	$\sigma_{LPN2,LPN3,LPN4}$	15.43	13.27	13.46
16a		18.20	16.36	16.34
15a		18.97	17.31	17.53
14a		19.38	17.95	17.85

[a]Fully optimized MP2/6-311++G(d,p) geometry.

and guarantee a good agreement between experiment and theory.

Next, within the 10-12.5 eV IE range, there is a large asymmetric group, in which only two experimental bands (B and C) can be identified and distinguished. Band B is centered at 10.85 eV and band C lies at 11.57 eV. Considering again the 2H-tautomer as the most abundant 5ATZ form and therefore taking the P3 results on 2H-5ATZ for the assignment, one can state that band B comes from the ionization of MO 21a, comprised of two opposing π orbitals in the tetrazole ring. Band C, however, is formed by the overlap of two σ lone pair orbitals, located in the tetrazole. P3 results give the correct asymmetry disposition (band C higher than band B), whereas OVFG B por-

Table 6: Calculated vertical ionization energies (VIE, in eV) of 2H-5ATZ

		2H-5ATZ		
		MP2	OVGF[a]	P3[a]
MO	Character	VIE	VIE	VIE
22a	$\pi_{N4-C5,N2-N3}$	9.80	9.23	9.51
21a	$\pi_{N1-N2,N3-N4}$	12.16	11.06	11.34
20a	σ_{LPN4}	13.01	11.35	11.72
19a	$\sigma_{LPN1,LPN3}$	13.69	11.66	11.99
18a	π_{C5-N6}	14.15	12.84	12.86
17a	$\sigma_{LPN1,LPN3,LPN4}$	15.70	13.67	13.99
16a		17.96	16.47	16.39
15a		18.61	16.55	16.59
14a		19.02	17.46	17.39

[a]Fully optimized MP2/6-311++G(d,p) geometry.

Table 7: Experimental vertical ionization energies (VIE, eV) and theoretical IE values (eV) for 5ATZ. MO stands for molecular orbital and ΔE for energy uncertainty (in eV).

Band	MO	VIE	ΔE	Previous[a]	Calc.[b]
A	22a	9.44	0.04	9.40	9.51
B	21a	10.85	0.07	10.87	11.34
C	20a	11.57	0.06	11.59	11.72
	19a				11.99
D	18a	12.66	0.03	12.81	12.86
E	17a	13.58	0.03	13.44	13.90

[a]Ref. [27]. [b]From P3 results on 2H-5ATZ.

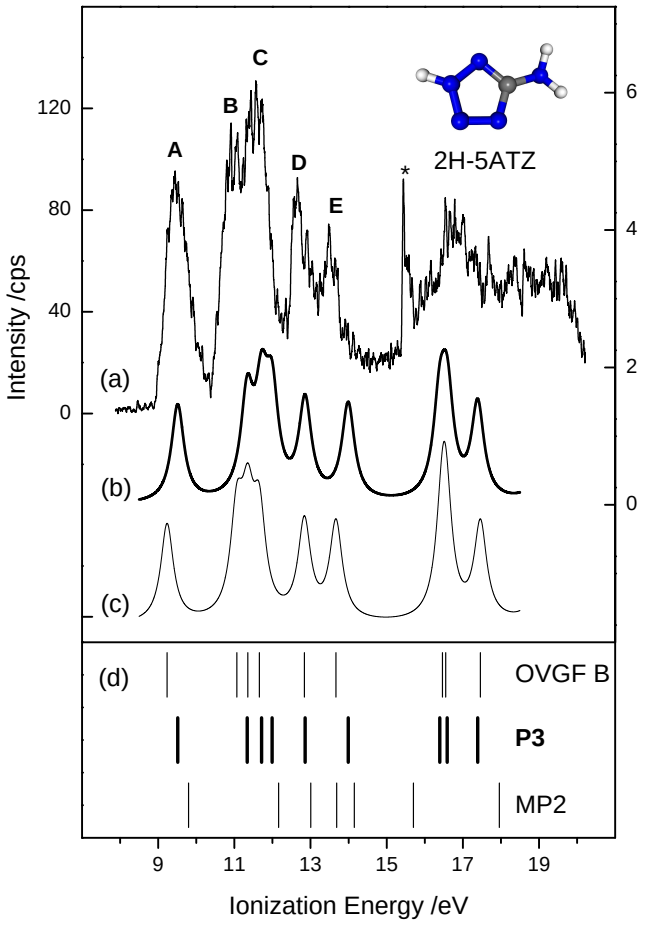

Figure 4: He(I) PE spectrum of 5ATZ, taken at 190 °C (a). The asterisk marks the N_2 peak from a controlled leak. Simulated PE spectrum of 2H-5ATZ, based on P3 (b) and OVGF B (c) results. VIEs of tetrazole 2H-5ATZ, using the MP2, P3 and OVGF B methods (d).

trays no asymmetry at all, with the three theoretical ionization lines equally spaced.

The following features appearing in the spectrum (bands D and E), within the 12.5-15 eV IE range, have similar narrow and peak-like shapes, which are known to be associated with ionizations of π type orbitals. In fact, according to our studies on the molecular orbitals contours (see Fig. 3), band D (12.66 eV) corresponds to the ionization of MO 18a, a π type orbital between the carbon and the nitrogen from the NH_2 group. The nearby band E (13.58 eV) is related to the ionization of MO 17a, which is comprised of several σ lone pairs on the tetrazole ring. The experimental IEs of bands A-E, the respective energy uncertainties and the P3 orbital energies for 2H-5ATZ are collected in Table 7. Comparison between the experimental values and the predicted VIEs on Tables 5 and 6 (considering only the first six HOMOs), leads to mean absolute differences (MADs) of 1.44, 0.24 and 0.26 eV, for 1H-5ATZ, and 1.41, 0.15 and 0.29 eV, for 2H-5ATZ, from MP2, OVGF and P3 calculations, respectively.

Although the P3 simulation of the 2H-tautomer perfectly describes the experimental spectrum until 15 eV, there are some additional features in this region that can only be explained by the inclusion of the 1H-5ATZ contribution: the shoulder at the right hand side of band A and the small band between peaks D and E.

The band patterns originating from the 1H-5ATZ simulation are markedly different from the ones obtained in the experimental spectrum, a fact that supports even more the known predominance of the 2H-tautomer in the gas-phase.

Finally, using the BPRs in Table 4, for 5ATZ at T=460 K, a simulated PE spectrum of 5-aminotetrazole, containing the two tautomers, was produced (Fig. 5, section (b)), which almost perfectly fits the experimental spectrum.

Further quantitative evaluation of the tautomeric stability from the experimental data implies the adoption of a proper deconvolution scheme which should take into account the spectrometer response function [54, 55]. In alternative, the determination of the exact Franck-Condon (FC) profile of the first band, through FC factors calculation, for both tautomers, would lead to almost exact tautomer population values [56]. However, these two approaches are outside the scope of the present work.

4.4. Thermal Decomposition of 5ATZ

Several spectra were recorded at increasing oven temperature, in small temperature steps and low heating rates, from an initial temperature near the melting point of 5ATZ (195-205

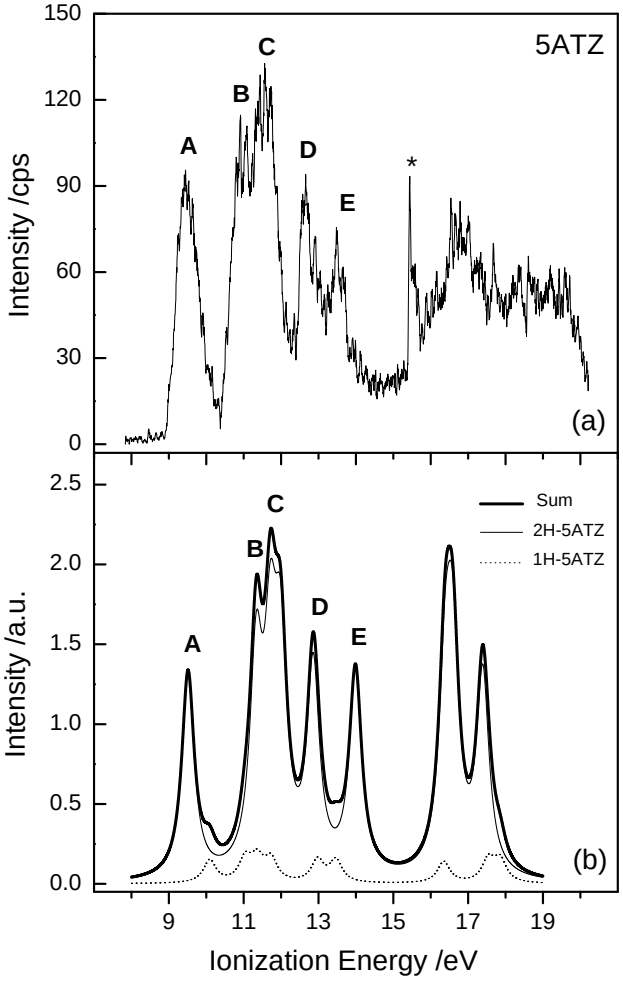

Figure 5: He(I) PE spectrum of 5ATZ, taken at 190 °C (a), and simulated outer-valence PE spectrum, based on P3/6-311++G(d,p) results (b). The asterisk marks the N_2 peak from a controlled leak.

°C). A typical thermal decomposition spectrum, taken at 245 °C, is shown in Fig. 6. Readily identified in this spectra are HN_3 and N_2, as the primary decomposition products, together with NH_2CN, HCN and 5ATZ vapor. A very low contribution from 5ATZ, which has its first broad band centered at 9.44 eV, indicates almost full decomposition.

Between 10 and 12 eV, the first bands of NH_2CN (VIE=10.65 eV [57]) and HN_3 (VIE=10.74 eV [58]) overlap, forming a wide band with a pronounced vibrational structure. Although the vibrational progression on top of this band appears to match the one from ammonia's first band (VIE=10.88 eV [59]), with an adiabatic ionization energy (AIE) of 10.15 eV [59] and vibrational spacing of 900 cm^{-1} [59], the excessive vibrational overlapping in this region does not allow us to unequivocally assign the progression to NH_3.

In the 12.0-13.5 IE range, there is a shoulder on the left side, followed by three sharp peaks and a narrow band. This shoulder corresponds to the second band of HN_3, centered at 12.2 eV, with 445 cm^{-1} vibrational intervals [58]. The three sharp peaks are associated with the ionization of the second HOMO

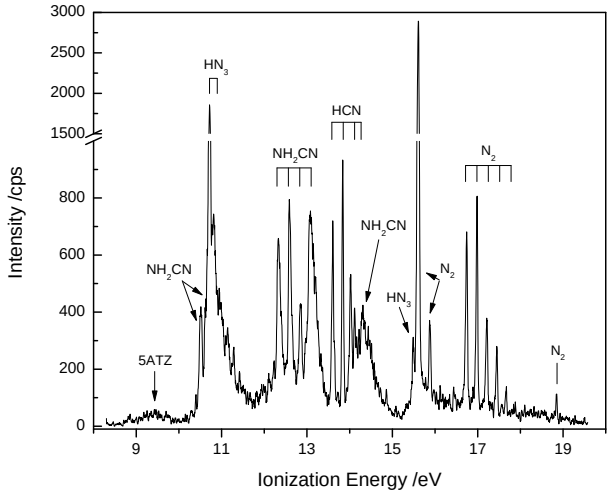

Figure 6: He(I) PE spectrum of the thermal decomposition of 5ATZ, taken at 245 °C.

of NH_2CN, centered at a 12.50 eV (middle peak, VIE) with associated vibrational structure appearing at ±2080 cm^{-1} [57] from this value. Finally, the narrow band at 12.98 eV is also assigned to NH_2CN, and is ascribed to the ionization of a non-bonding orbital of cyanamide.

The needle like peaks starting at 13.60 ($\Delta\nu \approx 1800$ cm^{-1}, due to the C≡N stretching) are unequivocally attributed to the ionization of HCN. The end of the vibrational progression of HCN is already on top of NH_2CN fourth band (VIE=14.23 eV [57]). Near the characteristic IE value of N_2 (15.60 eV [34]), one can also identify the third band of HN_3, at 15.47 eV [59].

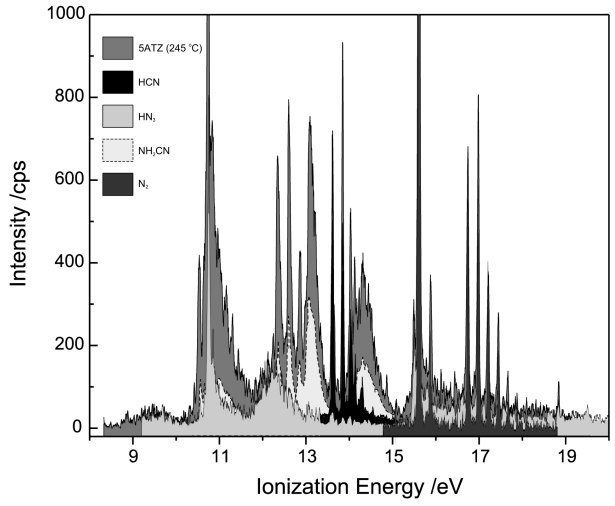

Figure 7: Detail of the He(I) PE spectrum of the thermal decomposition of 5ATZ (gray), taken at 245 °C, with estimated contributions from the decomposition species HCN (black), HN_3 (light gray), NH_2CN (lighter gray) and N_2 (dark gray).

These assignments of the thermal decomposition products for the overall spectral region are best interpreted in Fig. 7,

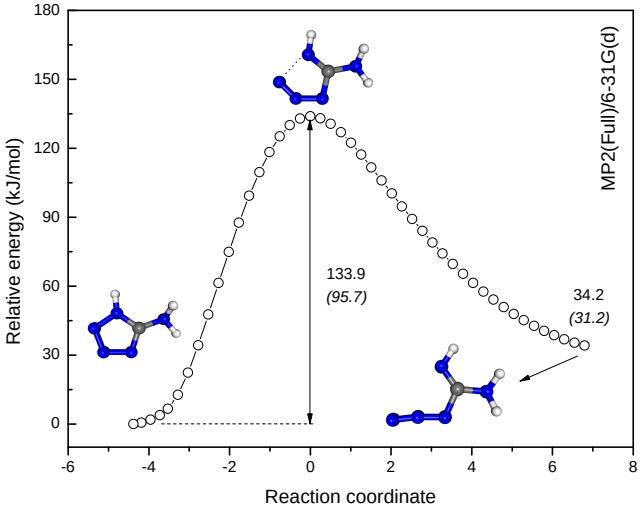

Figure 8: IRC calculations connecting 1H-5ATZ and the stable azide compound, obtained with MP2(Full)/6-31G(d). The relative energies of the TS and products, obtained with G2(MP2), are given in parentheses (in kJ/mol).

where the individual contributions of each product can be seen.

Four different routes can be used to explain the direct formation of the detected products, two for each tautomer. The formation of N_2 and a metastable CH_3N_3 molecule implies the transformation of 1H-5ATZ into an azide (azido-methanimidamide), which readily loses N_2, by the usual nitrogen elimination process that accompanies the pyrolysis of almost all organic azides. The barriers involved in this route are depicted in the IRC calculations of Fig. 8 and Fig. 9.

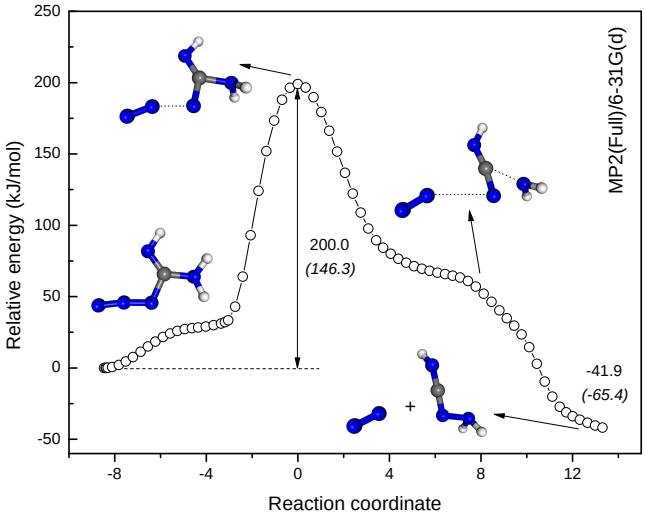

Figure 9: IRC calculations connecting the azide and N_2 plus the metastable CH_3N_3 compound, obtained with MP2(Full)/6-31G(d). The relative energies of the TS and products, obtained with G2(MP2), are given in parentheses (in kJ/mol).

The reaction path presented in Fig. 9 is very complex: the azide's NH_2 group undergoes rotation, followed by stretching of the N_2-N bond, which in turn breaks to give the unstable intermediate corresponding to the TS, 146.3 kJ/mol (calculated at the G2(MP2) level) above the energy of the initial azide. As N_2 moves farther away from the intermediate, the amino group bonds to the nitrogen end of the intermediate, stabilizing it and evolving to the final CH_3N_3 structure, a hydrazine derivative termed carboximidoylhydrazine. The sum of these two separated products is predicted to be more stable than the initial azide (-65.4 kJ/mol, from G2(MP2) results). This route clearly explains the formation of N_2 and the stable CH_3N_3 compound from 1H-5ATZ, but not the formation of HCN.

The direct formation of HN_3 and NH_2CN from the 1H-tautomer is explained by the elongation and breaking of the N3-N4 bond, followed by dissociation of the N1-C5 bond. Fig. 10 portrays this decomposition pathway, based on IRC calculations, obtained at the MP2(Full)/6-31G(d) level. Relatively to the initial product (1H-5ATZ) and the CH_3N_3 hydrazine from the previous route, N_2 plus cyanamide as final products are energetically less stable; in addition, the potential barrier for this reaction, calculated at the G2(MP2) level, is higher (204.7 kJ/mol) than the most energetic barrier calculated in the first decomposition route (146.3 kJ/mol).

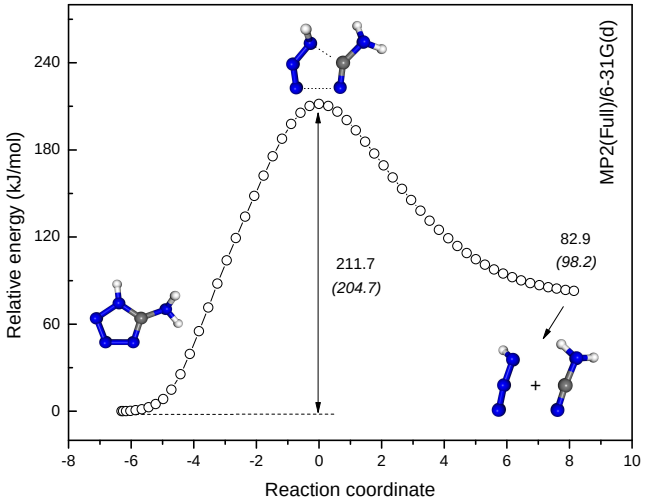

Figure 10: IRC calculations connecting 1H-5ATZ and HN_3 plus NH_2CN, obtained with MP2(Full) /6-31G(d). The relative energies of the TS and products, obtained with G2(MP2), are given in parentheses (in kJ/mol).

Concerning 2H-5ATZ thermal decomposition, two routes can also be envisaged. In contrast with 1H-5ATZ, the N_2 elimination in the 2H-tautomer occurs in a direct way, without the formation of any stable intermediate. The process starts with the rotation of the NH_2 group towards the hydrogenated side of the tetrazole, followed by the dissociation of the N2-N3 bond and elongation of the N4-C5 bond. The N4-C5 bond eventually breaks, releasing N_2 and leaving behind a short-lived CH_3N_3 carbene, named amino(diazenyl)methylidene. This reaction is depicted in the IRC of Fig. 11, where a potential barrier of approximately 149.6 kJ/mol (G2(MP2)) can be seen.

The formation of HN_3 from 2H-5ATZ decomposition is similar to the one from 1H-5ATZ. However, the dissociation starts from the hydrogenated side of the tetrazole instead, with the breaking of the N1-N2 bond, followed by elongation and breaking of the N4-C5 bond. The final products are again HN_3

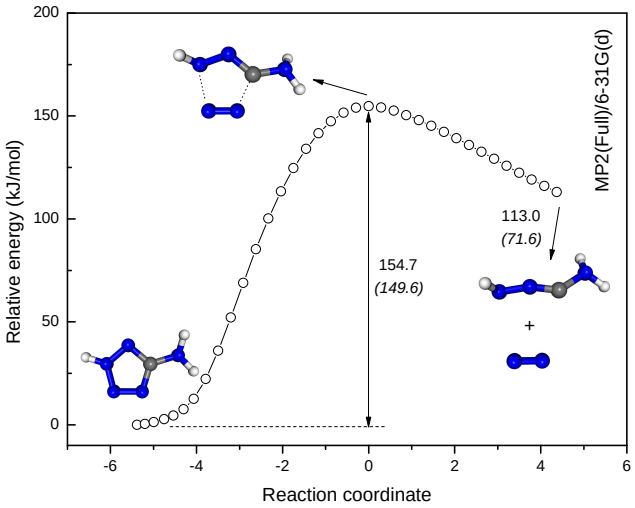

Figure 11: IRC calculations connecting 2H-5ATZ and N_2 plus amino(diazenyl)methylidene, obtained with MP2(Full)/6-31G(d). The relative energies of the TS and products, obtained with G2(MP2), are given in parentheses (in kJ/mol).

and NH_2CN and the IRC pathway that follows this reaction is presented in Fig. 12, where a energy barrier of 228.0 kJ/mol (G2(MP2)) arises.

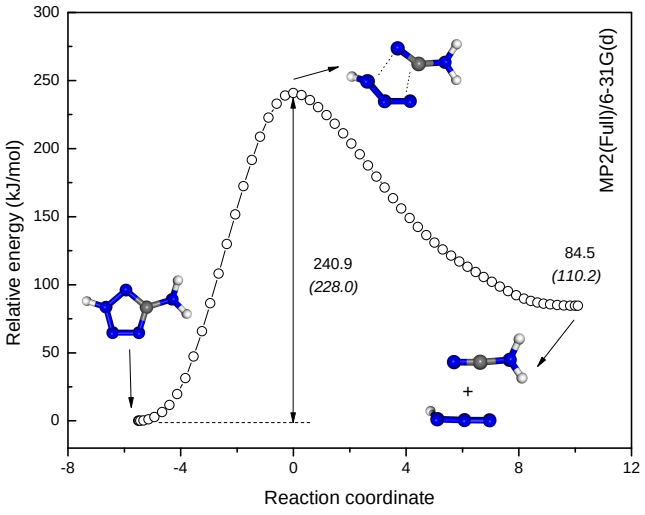

Figure 12: IRC calculations connecting 2H-5ATZ and HN_3 plus NH_2CN, obtained with MP2(Full) /6-31G(d). The relative energies of the TS and products, obtained with G2(MP2), are given in parentheses (in kJ/mol).

The sum of unimolecular processes that describe the thermal decomposition of 5ATZ is illustrated in Fig. 13. Associated with each step, we present the values for the potential energy barriers, obtained from the G2(MP2) energies at the stationary points of the PES, i.e. the energy differences between the reactants at each step and the corresponding TS. Also, the energies of all the products, relatively to the lowest energy tautomer 2H-5ATZ, are given above each structure. Results of our calculations are close to the data obtained by Kiselev and Gritsan [29], at the G3 level of theory.

The elimination of N_2 occurs as a one-step process in 2H-

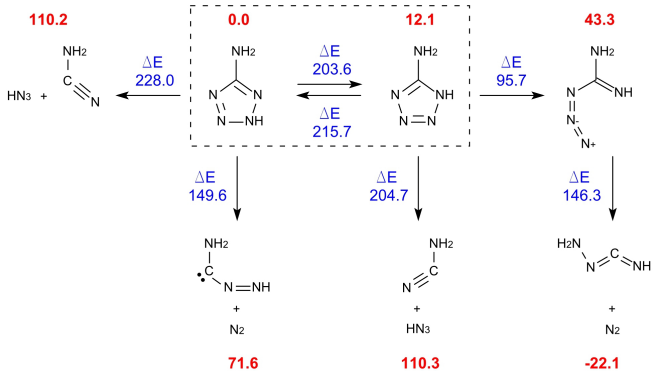

Figure 13: Proposed scheme for the thermal decomposition of gas-phase 5ATZ. G2(MP2) energies (in kJ/mol) relatively to the 2H-tautomer are given above each structure (in boldface) type font. ΔE represents the G2(MP2) energy barriers (in kJ/mol) between the product(s) and the preceding reactant.

5ATZ, in contrast with the N_2 elimination from 1H-5ATZ. The latter implies ring opening of the tetrazole moiety and formation of an azide, through a 95.7 kJ/mol barrier, followed by the N_2 loss (implying the transposition of a 146.3 kJ/mol energy barrier) and formation of the metastable CH_3N_3 molecule. The formation of HN_3 from both tautomers is also a one-step process, but it involves approximately 23.3 kJ/mol more in the case of 2H-5ATZ. Thus, HN_3 is formed primarily by the decomposition of 1H-5ATZ.

A second thermal decomposition stage, which should include the self-reaction of cyanamide [24] and the decomposition of HN_3, is outside the scope of our theoretical investigations. However, some insight concerning the formation of HCN can be given, supporting its clear assignment in the thermal decomposition spectra. Bearing this in mind, we have carried out some calculations on the CH_3N_3 carbene (resulting from 2H-5ATZ degradation) and its possible thermal decomposition. Fig. 14 shows the IRC calculations connecting it, the TS and another CH_3N_3 isomer, which is different from the previous hydrazine derivative obtained from the decomposition of the azide compound. This reaction consists on the rotation of the amino group and migration of the hydrogen atom that it is closer to the central carbon, in order to form the more stable isomer N-imino-methanimidamide, which involves a energy barrier of approximately 223.7 kJ/mol (G2(MP2)).

Comparison of this route to the one that leads to HN_3 and NH_2CN from 2H-5ATZ, readily shows that the latter is energetically more expensive than the combined scheme that leads to the formation of N_2 in the first stage and N-imino-methanimidamide in the second stage.

From this reaction, N-imino-methanimidamide is formed 89.9 kJ/mol below the initial carbene isomer, adopting a conformation with C_s symmetry, with all the atoms lying in plane and the terminal hydrogens positioned in a *cis* configuration. If the hydrogen atom from the imino group is allowed to approach the central nitrogen, by excitation of one of the vibrational modes, a reaction similar to the one depicted in Fig. 15 is possible.

Afterwards, the migration of the second hydrogen leads to

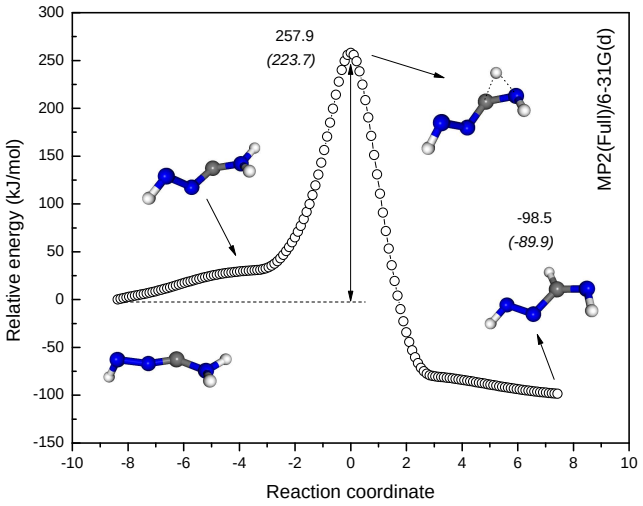

Figure 14: IRC calculations connecting the CH_3N_3 carbene (from 2H-5ATZ decomposition) and its isomer N-imino-methanimidamide, obtained with MP2(Full)/6-31G(d). The relative energies of the TS and products, obtained with G2(MP2), are given in parentheses (in kJ/mol).

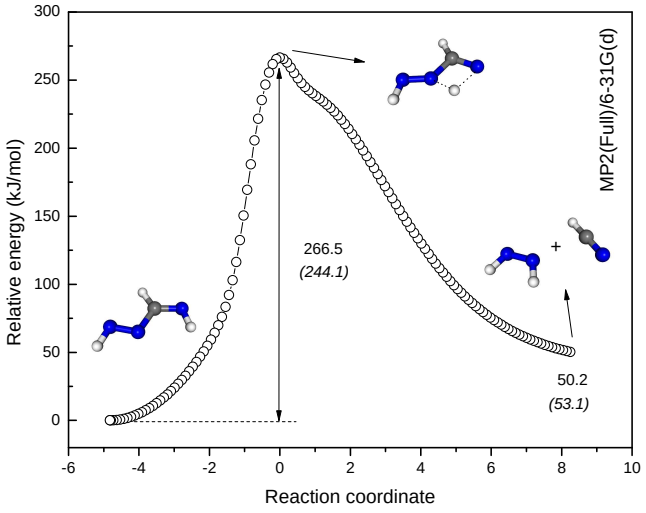

Figure 15: IRC calculations connecting N-imino-methanimidamide and HCN plus HNNH, obtained with MP2(Full)/6-31G(d). The relative energies of the TS and products, obtained with G2(MP2), are given in parentheses (in kJ/mol).

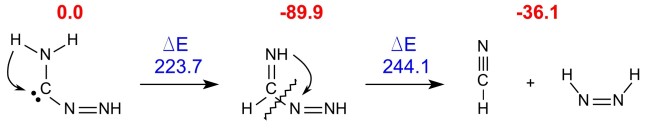

Figure 16: Proposed scheme for the thermal decomposition of the CH_3N_3 carbene. G2(MP2) energies (in kJ/mol) relatively to the carbene are given above each structure (in boldface type font). ΔE represents the G2(MP2) energy barriers (in kJ/mol) between the product(s) and the preceding reactant.

the direct formation of HCN and *cis*-diazene (HNNH), by elongation and breaking of the central N-C bond. This corresponds to a energy barrier of approximately 244.1 kJ/mol, calculated at the G2(MP2) level. Fig. 16 shows the mechanism underlying the proposed reaction scheme for the formation of HCN and HNNH. This is, in principle, a viable solution for the formation of HCN, as the maximum barrier involved in the mechanism is of the same order of magnitude as the other barriers present in the first stage of thermal decomposition of both tautomers. Finally, HNNH has a lifetime of the order of minutes in the gas phase at low pressure and is known to decompose into N_2 and H_2 [60].

5. Conclusions

For the first time, the analysis of the gas-phase PE spectrum of 5ATZ was accomplished, taking into account contributions from both 1H and 2H tautomers. The information retrieved from the computational results obtained within the electron propagator theory, is unequivocal in considering that this molecule adopts almost exclusively the 2H-form. Its HOMO VIE is 9.44±0.04 eV, and relates to the ionization of a π MO originated in the tetrazole ring. The ionization of both tautomers leads to structural changes in the hydrogens from the amino group, placing them in plane with the tetrazole ring and raising the tautomers' symmetry to C_s (from the previous C_1, in the neutral ground state).

In terms of 5ATZ thermal decomposition, results taken at 245 °C revealed N_2, HCN, NH_2CN, HN_3 and 5ATZ vapor as the main gaseous final products. Formation of N_2 from 1H-5ATZ implies the formation of azido-methanimidamide, which evolves into molecular nitrogen and carboximidoylhydrazine (HN=C=N-NH_2). The azide formation from 1H-5ATZ involves a 95.7 kJ/mol barrier and the subsequent nitrogen elimination from the azide engages a 146.3 kJ/mol barrier. The formation of HN_3 plus NH_2CN directly from 1H-5ATZ/2H-5ATZ requires the transposition of 204.7/228.0 kJ/mol barriers, respectively. This and the fact that the energy required for the 2H-1H conversion is less than 228.0 kJ/mol, favors the formation of HN_3 from the thermal degradation of predominantly the 1H-tautomer.

N_2 is eliminated from 2H-5ATZ without the formation of any intermediate, through a 149.6 kJ/mol barrier. This reaction leaves behind a short-lived carbene (amino(diazenyl)methylidene), which transforms into the more stable N-imino-methanimidamide, through a 223.7 kJ/mol amino hydrogen migration. The C-N central bond of this latter compound is then compelled to break through another hydrogen migration (244.1 kJ/mol barrier), leaving HCN and *cis*-diazene as the final products of dissociation.

In summary, the routes concerning only 2H-5ATZ can be used to explain the unimolecular thermal decomposition of gas-phase 5ATZ, because all the observed final products were predicted by theoretical calculations on the 2H-tautomer only, through accessible energy barriers (150-250 kJ/mol).

Acknowledgments

R. M. Pinto would like to acknowledge Fundação para a Ciência e Tecnologia (FCT) for the grant SFRH/BD/40308/2007.

Appendix A. Supplementary material

Energy-minimized cartesian coordinates (Table S1) and energies (Table S2) of all compounds under study, including intermediates and transition structures, calculated at the G2(MP2) level of theory.

References

[1] V. Ostrovskii, G. Koldobskii, R. Trifonov, in: A. R. Katritzky, C. A. Ramsden, E. F. Scriven, , R. J. Taylor (Eds.), Comprehensive Heterocyclic Chemistry III, Elsevier, Oxford, 2008, pp. 257 – 423.

[2] L. M. T. Frija, A. Ismael, M. L. S. Cristiano, Molecules 15 (2010) 3757–3774.

[3] J. Li, T. Ren, H. Liu, D. Wang, W. Liu, Wear 246 (2000) 130.

[4] J.-W. Lee, M.-C. Kang, J. J. Kim, J. Electrochem. Soc. 152 (2005) C827–C831.

[5] G. Steinhauser, T. M. Klapötke, Angew. Chem. Int. Ed. 47 (2008) 3330–3347.

[6] T. M. Klapötke, C. M. Sabate, Chem. Mater. 20 (2008) 3629.

[7] T. M. Klapötke, J. Stierstorfer, J. Am. Chem. Soc. 131 (2009) 1122.

[8] Y. Hashimoto, R. Ohashi, Y. Kurosawa, K. Minami, H. Kaji, K. Hayashida, H. Narita, S. Murata, J. Cardiovasc. Pharmacol. 31 (1998) 568–575.

[9] A. De Sarro, D. Ammendola, M. Zappala, S. Grasso, G. De Sarro, Antimicrob. Agents Chemother. 39 (1995) 232–237.

[10] R. J. Herr, Bioorg. Med. Chem. 10 (2002) 3379.

[11] L. Myznikov, A. Hrabalek, G. Koldobskii, Chem. Heterocycl. Compd. 43 (2007) 1.

[12] A. Mazurek, N. Sadlej-Sosnowska, Chem. Phys. Lett. 330 (2000) 212–218.

[13] R. Trifonov, I. Alkorta, V. Ostrovskii, J. Elguero, J. Mol. Struct.: Theochem 668 (2004) 123–132.

[14] R. M. Balabin, J. Chem. Phys. 131 (2009) 154307.

[15] J. Elguero, C. Marzin, J. D. Roberts, J. Org. Chem. 39 (1974) 357–363.

[16] D. S. Wofford, D. M. Forkey, J. G. Russell, J. Org. Chem. 47 (1982) 5132–5137.

[17] M. Sokolova, V. Melnikov, V. Ostrovskii, G. Koldobskii, A. Melnikov, B. Gidaspov, Z. Organ. Khim. 11 (1975) 1744–1749.

[18] G. Maier, J. Eckwert, A. Bothur, H. Reisenauer, C. Schmidt, Liebigs Ann. (1996) 1041–1053.

[19] A. Gomez-Zavaglia, I. D. Reva, L. Frija, M. L. Cristiano, R. Fausto, J. Phys. Chem. A 109 (2005) 7967–7976.

[20] M. H. Palmer, I. Simpson, J. R. Wheeler, Z. Naturforsch. 36a (1981) 1246–1252.

[21] A. Rażyńska, A. Tempczyk, E. Maliński, J. Szafranek, Z. Grzonka, J. Chem. Soc. Perkin Trans. II (1983) 379.

[22] M. Wong, R. Leungtoung, C. Wentrup, J. Am. Chem. Soc. 115 (1993) 2465–2472.

[23] S. Levchik, O. Ivashkevich, A. Balabanovich, A. Lesnikovich, P. Gaponik, L. Costa, Thermoch. Acta 207 (1992) 115 – 130.

[24] T. B. Brill, H. Ramanathan, Combust. Flame 122 (2000) 165–171.

[25] A. Lesnikovich, O. Ivashkevich, S. Levchik, A. Balabanovich, P. Gaponik, A. Kulak, Thermochim. Acta 388 (2002) 233–251.

[26] A. A. Paletsky, N. V. Budachev, O. P. Korobeinichev, Kinet. Catal. 50 (2009) 627–635.

[27] Z. Sun, X.-Q. Zeng, W.-G. Wang, M.-F. Ge, D.-X. Wang, Acta Chim. Sinica 64 (2006) 218–222.

[28] J. Zhang, L. Feng, S. Zhang, T. Zheng, H. Zheng, J. Mol. Model. 14 (1992) 403 – 408.

[29] V. G. Kiselev, N. P. Gritsan, J. Phys. Chem. A 113 (2009) 3677–3684.

[30] K. W. Paul, M. M. Hurley, K. K. Irikura, J. Phys. Chem. A 113 (2009) 2483–2490.

[31] I. Novak, B. Kovač, L. Klasinc, V. A. Ostrovskii, Spectroc. Acta Part A 59 (2003) 1725–1731.

[32] I. L. Zaytseva, A. B. Trofimov, J. Schirmer, O. Plekan, V. Feyer, R. Richter, M. Coreno, K. C. Prince, J. Phys. Chem. A 113 (2009) 15142–15149.

[33] A. Morris, N. Jonathan, J. M. Dyke, P. D. Francis, N. Keddar, J. D. Mills, Rev. Sci. Instrum. 55 (1984) 172–181.

[34] K. Kimura, Handbook of HeI photoelectron spectra of fundamental organic molecules : ionization energies, ab initio assignments, and valence electronic structure for 200 molecules, Japan Scientific Societies Press ; Halsted Press, Tokyo; New York, 1981.

[35] L. S. Cederbaum, J. Phys. B 8 (1975) 290.

[36] W. von Niessen, J. Schirmer, L. S. Cederbaum, Comput. Phys. Rep. 1 (1984) 57–125.

[37] J. V. Ortiz, J. Chem. Phys. 104 (1996) 7599–7605.

[38] A. B. Trofimov, J. Schirmer, V. B. Kobychev, A. W. Potts, D. M. P. Holland, L. Karlsson, J. Phys. B 39 (2006) 305.

[39] A. Chrostowska, T. X. M. Nguyen, A. Dargelos, S. Khayar, A. Graciaa, J. Guillemin, J. Phys. Chem. A 113 (2009) 2387–2396.

[40] C. C. J. Roothaan, Rev. Mod. Phys. 23 (1951) 69–89.

[41] C. Møller, M. S. Plesset, Phys. Rev. 46 (1934) 618–622.

[42] R. Parr, Y. Weitao, Density-Functional Theory of Atoms and Molecules, Oxford University Press, New York, 1994.

[43] R. Krishnan, J. S. Binkley, R. Seeger, J. A. Pople, J. Chem. Phys. 72 (1980) 650–654.

[44] A. Becke, J. Chem. Phys. 98 (1993) 5652, 5648.

[45] C. Lee, W. Yang, R. G. Parr, Phys. Rev. B 37 (1988) 785–789.

[46] L. A. Curtiss, K. Raghavachari, J. A. Pople, J. Chem. Phys. 98 (1993) 1293–1298.

[47] R. M. Balabin, J. Chem. Phys. 129 (2008) 164101.

[48] R. M. Balabin, J. Phys. Chem. A 114 (2010) 3698–3702.

[49] G. Lendvay, I. Mayer, Chem. Phys. Lett. 297 (1998) 365–373.

[50] M. J. Frisch, G. W. Trucks, H. B. Schlegel, G. E. Scuseria, M. A. Robb, J. R. Cheeseman, G. Scalmani, V. Barone, B. Mennucci, G. A. Petersson, H. Nakatsuji, M. Caricato, X. Li, H. P. Hratchian, A. F. Izmaylov, J. Bloino, G. Zheng, J. L. Sonnenberg, M. Hada, M. Ehara, K. Toyota, R. Fukuda, J. Hasegawa, M. Ishida, T. Nakajima, Y. Honda, O. Kitao, H. Nakai, T. Vreven, J. A. Montgomery, Jr., J. E. Peralta, F. Ogliaro, M. Bearpark, J. J. Heyd, E. Brothers, K. N. Kudin, V. N. Staroverov, R. Kobayashi, J. Normand, K. Raghavachari, A. Rendell, J. C. Burant, S. S. Iyengar, J. Tomasi, M. Cossi, N. Rega, J. M. Millam, M. Klene, J. E. Knox, J. B. Cross, V. Bakken, C. Adamo, J. Jaramillo, R. Gomperts, R. E. Stratmann, O. Yazyev, A. J. Austin, R. Cammi, C. Pomelli, J. W. Ochterski, R. L. Martin, K. Morokuma, V. G. Zakrzewski, G. A. Voth, P. Salvador, J. J. Dannenberg, S. Dapprich, A. D. Daniels, . Farkas, J. B. Foresman, J. V. Ortiz, J. Cioslowski, D. J. Fox, Gaussian 09 Revision A.02, 2009. Gaussian Inc. Wallingford CT 2009.

[51] A. W. Potts, D. M. P. Holland, A. B. Trofimov, J. Schirmer, L. Karlsson, K. Siegbahn, J. Phys. B 36 (2003) 3129.

[52] Z. X. Chen, J. M. Xiao, H. M. Xiao, Y. N. Chiu, J. Phys. Chem. A 103 (1999) 8062–8066.

[53] A. N. Chermahini, M. Nasr-Esfahani, Z. Dalirnasab, H. A. Dabbagh, A. Teimouri, J. Mol. Struct. (THEOCHEM) 820 (2007) 7–11.

[54] D. Sprenger, O. Anderson, Fresen. J. Anal. Chem. 341 (1991) 116–120.

[55] J. Allen, F. Grimm, Chem. Phys. Lett. 66 (1979) 72–78.

[56] K. B. Bravaya, O. Kostko, S. Dolgikh, A. Landau, M. Ahmed, A. I. Krylov, J. Phys. Chem. A 114 (2010) 12305–12317.

[57] H. Stafast, H. Bock, Chem. Ber. 107 (1974) 1882–1890.

[58] J. H. D. Eland, Phil. Trans. Roy. Soc. Lond. A 268 (1970) 87–96.

[59] A. W. Potts, W. C. Price, Proc. R. Soc. Lond. A. 326 (1972) 181–197.

[60] D. C. Frost, S. T. Lee, C. A. McDowell, N. P. C. Westwood, J. Chem. Phys. 64 (1976) 4719–4729.